Experimental Investigation of the Thermal Emission Cross Section of Nanoresonators Using Hierarchical Poisson-Disk Distributions

Denis Langevin,[1] Clément Verlhac,[1] Julien Jaeck,[1] Loubnan Abou-Hamdan,[1,3] Eva Taupeau,[1] Baptiste Fix,[1]
Nathalie Bardou,[2] Christophe Dupuis,[2] Yannick De Wilde,[3] Riad Haïdar,[1] and Patrick Bouchon[1,*]
[1]*DOTA, ONERA, Université Paris-Saclay, F-91123 Palaiseau, France*
[2]*Center for Nanosciences and Nanotechnology (C2N) - CNRS, Université Paris-Saclay,*
10 Boulevard Thomas Gobert, 91120 Palaiseau, France
[3]*Institut Langevin, ESPCI Paris, PSL University, CNRS, 1 rue Jussieu, F-75005 Paris, France*

(Received 31 January 2023; accepted 8 December 2023; published 22 January 2024; corrected 21 February 2024)

Effective cross sections of nano-objects are fundamental properties that determine their ability to interact with light. However, measuring them for individual resonators directly and quantitatively remains challenging, particularly because of the very low signals involved. Here, we experimentally measure the thermal emission cross section of metal-insulator-metal nanoresonators using a stealthy hyperuniform distribution based on a hierarchical Poisson-disk algorithm. In such distributions, there are no long-range interactions between antennas, and we show that the light emitted by such metasurfaces behaves as the sum of cross sections of independent nanoantennas, enabling direct retrieval of the single resonator contribution. The emission cross section at resonance is found to be on the order of $\lambda_0^2/3$, a value that is nearly 3 times larger than the theoretical maximal absorption cross section of a single particle, but remains smaller than the maximal extinction cross section. This measurement technique can be generalized to any single resonator cross section, and we also apply it to a lossy dielectric layer.

DOI: 10.1103/PhysRevLett.132.043801

Optical nanoantennas, often inspired by radio frequency designs of classical antennas [1], have been used to tame electromagnetic wave properties at optical wavelengths far below the diffraction limit [2–6]. The interactions of single nanoantennas with light can be of great interest to a multitude of light applications [7–14], but they can also be used as building blocks (meta-atoms) for larger metasurfaces [15,16]. Among the fundamental properties of single objects are their effective absorption and scattering cross sections, the sum of which is the extinction cross section [17,18]. These quantities describe the single object's ability to interact with light at a given frequency, but are often complex to quantify experimentally [19,20].

In practice, the direct measurement of the absorption cross section has so far remained rather elusive [21]. As a result, the absorption cross section is typically obtained by taking the difference between the extinction and scattering cross sections. The emission cross section can also be introduced based on the local polarized emissivity density that is linked to absorptivity by Kirchhoff's law [22]. Direct measurements of either infrared absorption or infrared thermal emission of single objects has been previously demonstrated, but the signal is very low, particularly in comparison with the emitting background [12,23–26]. Determining absorption and emission cross sections of single objects is of the utmost importance for applications such as thermoplasmonics [27], energy conversion, [28,29] and metaemitters with tailored emission (polarization, spectral) [30–34].

In this Letter, we measure, both directly and quantitatively, the thermal emission cross section of nanoresonators arranged as a correlated disorder distribution. The metasurface is built following a hierarchical Poisson-disk algorithm with various densities that gives a stealthy hyperuniform distribution. For low densities, we show that the thermal emission is linearly dependent on the density of nanoantennas, thus behaving as an independent combination. In that case, we measure the sum of the individual antennas' thermal emission cross sections. These measurements are shown to be in good agreement with electromagnetic computations on a single nanoantenna. Finally, we demonstrate that our experimental protocol can be applied to a lossy insulating material and demonstrate its robustness at lower temperature.

The various electromagnetic cross sections of a single nano-object on an opaque substrate are illustrated in Figs. 1(a)–1(c). The scattering cross section σ_{scat} and the absorption cross section σ_{abs} are shown for the case of a normally incident monochromatic plane wave. Their sum gives the well-known extinction cross section $\sigma_{\text{ext}} = \sigma_{\text{abs}} + \sigma_{\text{scat}}$. At a temperature T, the nano-object emits light due to thermal fluctuations according to Planck's law. Thus, we introduce the emission cross section σ_{em} that describes its ability to emit light for a given wavelength λ, direction of emission $\vec{u}$, and polarization. The local form of Kirchhoff's law equates the absorption cross section to the emission cross section for similar conditions, i.e., $\sigma_{\text{em}}(\vec{u}, \lambda) = \sigma_{\text{abs}}(\vec{u}, \lambda)$ [22].

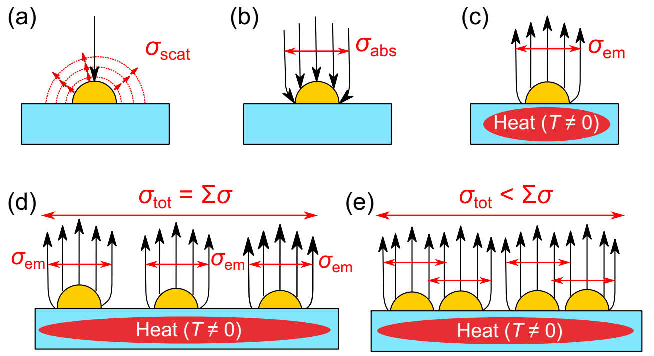

FIG. 1. Illustration of the (a) scattering, (b) absorption, and (c) emission cross sections for a nano-object. (d) Nonoverlapping cross sections. (e) Overlapping cross sections.

An object's emission cross section in a given direction $\vec{u}$ at a wavelength λ is defined by

$$\sigma_{\mathrm{em}}(\vec{u},\lambda) = \int_V \eta(\vec{u},\vec{r},\lambda) d^3\vec{r}, \qquad (1)$$

where $\eta(\vec{u},\vec{r},\lambda)$ is the local spectral directional emissivity at position $\vec{r}$ in the object. This is equal to the absorptivity of the object and can be computed using the object's local permittivity [22].

Figures 1(d) and 1(e) extend this illustration to assemblies of nano-objects emitting light. In the first case, the nano-objects are sufficiently far apart so that no interactions may arise. The total emission cross section $\sigma_{\mathrm{em}}^{(\mathrm{tot})}$ is then given by the sum of the individual emission cross sections $\sum \sigma_{\mathrm{em}}^{(\mathrm{res})}$. In the second case [Fig. 1(e)], the resonators are much closer to one another and can no longer be considered independent. Therefore, the individual cross sections become spatially overlapping, giving rise to near-field interactions so that $\sigma_{\mathrm{em}}^{(\mathrm{tot})} \neq \sum \sigma_{\mathrm{em}}^{(\mathrm{res})}$. In most situations, the overlap of cross sections leads to a loss of efficiency, i.e., $\sigma_{\mathrm{em}}^{(\mathrm{tot})} < \sum \sigma_{\mathrm{em}}^{(\mathrm{res})}$. However, hybridized modes may appear and generate constructive interferences, leading to $\sigma_{\mathrm{em}}^{(\mathrm{tot})} > \sum \sigma_{\mathrm{em}}^{(\mathrm{res})}$. In any case, the total far-field emission obviously remains below the fundamental limit set by the fact that the emissivity of any object cannot be larger than 1.

Periodic arrays of nanoresonators are commonly employed to reach this theoretical limit, in which complete absorption of incoming light is readily achieved by reaching a critical coupling condition [35]. However, the array period, along with diffraction effects, plays a major role in the overall behavior of the sample, concealing the contribution of the individual resonators [36]. The emission cross section of a nanoantenna in an array of period d at critical coupling can be written as $\sigma_{\mathrm{em}}^{(\mathrm{tot})} = d^2$ at resonance. Consequently, the measurement of electromagnetic cross sections can only be effected in the case of a single resonator or an aperiodic resonator distribution.

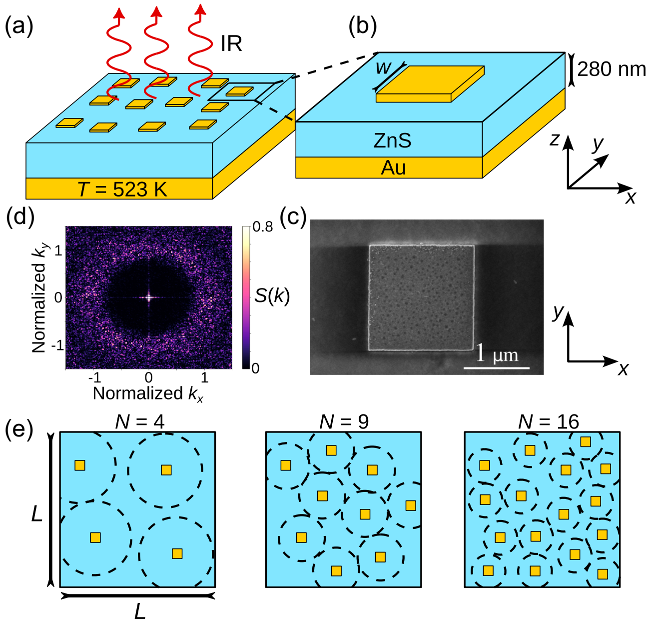

FIG. 2. (a) Scheme of the sample, with the overall distribution. (b) Scheme of the single resonator geometry. (c) Scanning electron microscope top view image of a single resonator ($w = 1.6$ μm). (d) Structure factor of a distribution where $N = 40\,000$ and $L = 1$ mm. (e) Examples of three consecutive states of the resonator distribution, after N steps. The dashed circles are exclusion zones where no additional antennas can be placed.

In what follows, the emission response of hyperuniform disordered metasurfaces using metal-insulator-metal (MIM) resonators as building blocks is investigated, as depicted in Fig. 2. This type of antenna, commonly used in metasurface design, acts as a Fabry-Perot nanocavity [35,37]. Here, the MIM resonators consist of square gold antennas placed on top of a zinc sulfide (ZnS) layer with a metallic backplate. The thickness of the dielectric layer is 280 nm, and the antenna width w is chosen so that the resonance wavelength is in the long-wave infrared spectral range (8–12 μm). The metallic layer thickness is chosen to be significantly larger than the skin depth of the metal. A scheme of this resonator structure is shown in Figs. 2(a)–2(c), together with an SEM image of a single resonator.

The stealthy hyperuniform disordered distribution is obtained following a hierarchical Poisson-disk algorithm [38]. This algorithm resembles random sequential adsorption [39], in that it builds the distribution gradually by randomly picking new positions one by one, only adding a new position to the distribution if it satisfies a predefined separation distance with respect to all previously chosen positions. The hierarchical Poisson-disk algorithm introduces a large exclusion distance between new positions that is gradually decreased as the distribution density D increases.

This ensures that the algorithm can place a precisely chosen number of resonators N, rather than stopping when the exclusion zones overlap, and that the first n chosen positions are also hyperuniform, for any $n < N$. Thus, once a design of given density D is created, designs of any density lower than D can be retrieved by simply taking a subset of the densest distribution. This guarantees that the density variations between samples are only caused by adding or removing resonators from an existing distribution, without changing the positions of other resonators in the process. This type of distribution minimizes the long-range correlations between resonators, thereby precluding the contribution of structural effects of the distribution on the signal [40,41]. A way to characterize hyperuniformity is through the structure factor of the resonator distribution that can be computed for any distribution $\{R\}_j$ of N points as [41]

$$S(\vec{k}) = \frac{1}{N}\sum_{j_1}\sum_{j_2}\exp^{-i\vec{k}(\vec{R}_{j_1}-\vec{R}_{j_2})}.$$

The structure factor for a hierarchical Poisson-disk distribution with $N = 40\,000$ is plotted in Fig. 2(d). The dark central area in this structure factor is a typical characteristic of a stealthy hyperuniform distribution [42]. The absence of high intensity peaks outside of the dark area indicates that there are no long-range correlations between positions. The degree of stealthiness χ is a parameter that is commonly used to characterize hyperuniform distributions [43], as it depends on the size of the low S area visible in Fig. 2(d). The distributions used in this Letter typically have $\chi \sim 0.3$ (see Supplemental Material [44]).

An example of the state of the distribution given by the hierarchical Poisson-disk algorithm at different steps is shown in Fig. 2(e). The overall resonator density D of each sample is given by the number of resonators per sample area: $D = N/L^2$. We can identify samples by their resonator density D, or by the period $L_{\mathrm{eq}} = 1/\sqrt{D}$ of its equivalent periodic array of the same density.

The infrared thermal emission of disordered MIM metasurfaces with various densities, heated to $T = 523$ K with a Linkam THMS600 heating stage, is collected around normal incidence by a parabolic mirror. The heated metasurface acts as an external source for a Fourier-transform infrared spectrometer that measures its emission spectrum (see Supplemental Material [44]).

The studied metasurfaces consist of square-patch MIM antennas of width $w = 1.6$ μm distributed according to the hierarchical Poisson-disk distribution at various densities. The emissivity spectra of metasurfaces with resonator density $D = 1/64$ and $D = 1/256$ μm^{-2} are shown in Fig. 3(a), with scanning electron microscope (SEM) images illustrating the distribution. Both metasurfaces exhibit a resonance at the same wavelength $\lambda_r = 8.7$ μm, and as expected, the measured emissivity for the denser metasurface is higher.

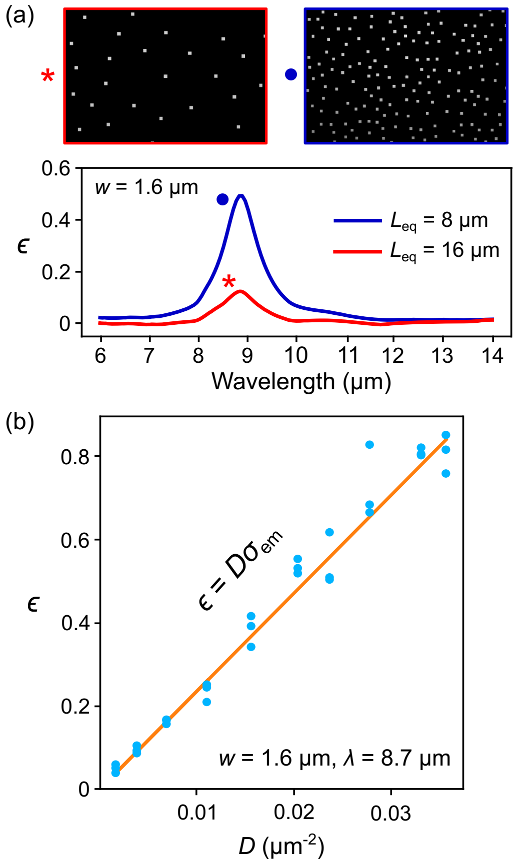

FIG. 3. (a) Measured emissivity ϵ spectra of the hyperuniform disordered metasurface with resonator density $D = 1/64$ μm^{-2}, or equivalent period $L_{\mathrm{eq}} = 8$ μm (blue curve) and $D = 1/256$ μm^{-2}, or $L_{\mathrm{eq}} = 16$ μm (red curve). The spectra were measured at $T = 523$ K. The SEM images of the two metasurfaces are shown above at the same magnification. (b) Emissivity as a function of the density of the metasurface at resonance wavelength $\lambda_r = 8.7$ μm for several measurements (blue dots). The linear regression slope (orange line) gives the emission cross section σ_{em} at $\lambda_r = 8.7$ μm.

At each wavelength λ, the emission cross section $\sigma_{\mathrm{em}}(\lambda)$ can be extracted from the slope of the linear regression of the emissivity as a function of density. Indeed, as illustrated in Fig. 1(d), for independent nanoemitters, the emissivity is given by $\epsilon(\lambda) = \sum_{i=1}^{N}\sigma_{\mathrm{em}}(\lambda)/L^2 = \sigma_{\mathrm{em}}(\lambda)D$. This behavior is illustrated at the resonance wavelength in Fig. 3(b). The measured value gives $\sigma_{\mathrm{em}}(\lambda_r) = 24$ μm^2 for the resonant wavelength of 8.7 μm. This means that $\sigma_{\mathrm{em}}(\lambda_r) \sim (\lambda_r^2/3)$. This order of magnitude is to be expected for a nanoresonator on a reflective backplate [19,51], but this value is higher than the maximum theoretical value for a single resonant dipolar particle, i.e., $\sigma_{\mathrm{abs}}^{\mathrm{dipole}} = (3\lambda^2/8\pi)$ [52,53] (see Supplemental Material [44] for the derivation).

Following the same process at each wavelength, we obtain the emission cross section spectra, which are shown

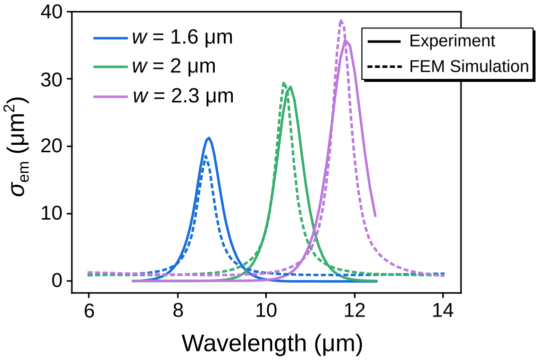

FIG. 4. Comparison of measured and simulated emission cross section spectra. The measurements correspond to a resonator distribution of density $L_{eq} = 16$ μm, while the electromagnetic simulations are for single resonators using perfectly matched layers.

in Fig. 4 for various resonator geometries. This shows that both the resonance wavelength and the maximum cross section increase with increasing resonator width w, as expected [24].

To further validate these experimental measurements, we performed finite-element method (FEM) electromagnetic simulations (COMSOL Multiphysics [54]) of single resonators using perfectly matched layers. The emission cross section of an individual square MIM resonator was retrieved and compared to the experimental measurements in Fig. 4. The FEM simulations are found to be in very good agreement with the experimental measurements, both in resonance wavelength and magnitude.

The methodology presented thus far can be extended to other systems, particularly to samples in which material absorption is present in dielectric layers, which we illustrate in what follows. To this end, the zinc sulfide layer is replaced by a silicon oxide (SiO_2) layer of thickness $h_{SiO_2} = 180$ nm that exhibits a large absorption above 8 μm. The distribution and MIM antenna geometry are rigorously identical to that of Fig. 3. First, we show in Fig. 5(a) that the distribution's emissivity can be robustly measured at lower temperatures (down to 348 K), despite the fact that the signal-to-noise ratio decreases with decreasing temperature. The shown emissivity spectra were obtained on the densest distribution with an equivalent period $L_{eq} = 5.3$ μm. In this case, two emission peaks are observed at $\lambda_{res} = 5.6$ and $\lambda_{res} = 10.2$ μm, both of which correspond to the fundamental Fabry-Perot resonance of the MIM cavity, as the result of strong variations in SiO_2's permittivity in the 8–12 μm spectral range [55]. In particular, the broad asymmetric shape of the second peak at 10.2 μm is directly linked to these variations. The first resonance is expectedly at a lower wavelength than that of the ZnS MIM cavity due to the lower real part of the dielectric function of SiO_2.

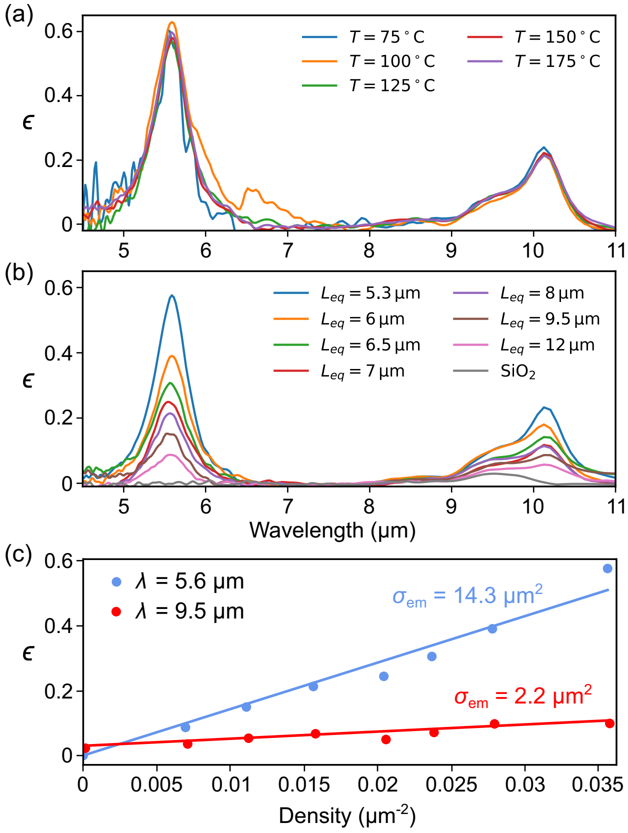

FIG. 5. SiO_2 hyperuniform metasurface: (a) Measured emissivity spectra of the hyperuniform disordered metasurface with resonator equivalent period $L_{eq} = 5.3$ μm for various temperatures. (b) Measured emissivity spectra for various density D at $T = 175\,°C$. (c) Emissivity as a function of the density of the metasurface at $\lambda_1 = 5.6$ μm (blue dots) and $\lambda_2 = 9.5$ μm (orange dots). The continuous lines show the linear regression $\epsilon = \sigma_{em} D + \epsilon_{SiO_2}$.

The behavior of the emissivity at various resonator densities and at zero density (i.e., the bare SiO_2 layer) is illustrated in Fig. 5(b), revealing the same trend observed with the ZnS samples. We extract the emission cross section at $\lambda_{res} = 5.6$ μm from the slope of the linear regression of emissivity as a function of density [Fig. 5(c)], which gives $\sigma_{em} = 14.3\ \mu m^2 \simeq 0.46\lambda_{res}^2$. Taken relative to the wavelength, this value is larger than that obtained for the ZnS MIM cavity.

As soon as the SiO_2 is absorbing, the linear regression has to account for the residual emissivity of the dielectric layer as follows:

$$\epsilon(\lambda) = \sigma_{em}(\lambda) D + \epsilon_{SiO_2}(\lambda).$$

The y intercept of the linear regression in this case gives the residual emissivity ϵ_{SiO_2} due to the absorbing SiO_2 layer. Performing the linear regression at $\lambda = 9.5$ μm, which is close to the absorption resonance of SiO_2, we find $\sigma_{em} = 2.2\ \mu m^2 \simeq (\lambda^2/40)$ and $\epsilon_{SiO_2} = 0.03$.

In summary, we have presented a protocol based on hyperuniform distributions to quantitatively measure single resonator cross sections using large distribution far-field measurements. We applied this protocol to emission cross sections of MIM resonator distributions, for which we obtained $\sigma_{\mathrm{em}} = 24\ \mu\mathrm{m}^2$ for a MIM cavity with a ZnS insulating layer. These results were found to be in fair agreement with FEM simulations of single resonators, confirming that our measurement protocol gives direct access to the single resonator emission cross section. Finally, we extended our measurement protocol to the case of an absorbing insulating layer, in which the robustness of the technique was also validated by variable temperature measurements carried out at sample temperatures as low as 75 °C. In this case, the utilized linear regression also accounts for the residual material absorption of the sample without any patterning. The intimate knowledge of the emission cross section is a first step to predict the infrared appearance of metasurfaces as seen by infrared detection systems [56].

This work was done within the C2N micronanotechnologies platforms and partly supported by the RENATECH Network and the General Council of Essonne. D. L. was also supported by a DGA-AID scholarship.

---

[*] patrick.bouchon@onera.fr

[1] B. A. Munk, *Finite Antenna Arrays and FSS* (John Wiley & Sons, New York, 2003).

[2] M. L. Brongersma, Engineering optical nanoantennas, Nat. Photonics **2**, 270 (2008).

[3] L. Novotny and N. Van Hulst, Antennas for light, Nat. Photonics **5**, 83 (2011).

[4] P. Biagioni, J.-S. Huang, and B. Hecht, Nanoantennas for visible and infrared radiation, Rep. Prog. Phys. **75**, 024402 (2012).

[5] A. E. Krasnok, I. S. Maksymov, A. I. Denisyuk, P. A. Belov, A. E. Miroshnichenko, C. R. Simovski, and Y. S. Kivshar, Optical nanoantennas, Phys. Usp. **56**, 539 (2013).

[6] A. F. Koenderink, Single-photon nanoantennas, ACS Photonics **4**, 710 (2017).

[7] F. Neubrech, A. Pucci, T. W. Cornelius, S. Karim, A. García-Etxarri, and J. Aizpurua, Resonant plasmonic and vibrational coupling in a tailored nanoantenna for infrared detection, Phys. Rev. Lett. **101**, 157403 (2008).

[8] M. L. Brongersma, N. J. Halas, and P. Nordlander, Plasmon-induced hot carrier science and technology, Nat. Nanotechnol. **10**, 25 (2015).

[9] S. A. Mann, S. Z. Oener, A. Cavalli, J. E. Haverkort, E. P. Bakkers, and E. C. Garnett, Quantifying losses and thermodynamic limits in nanophotonic solar cells, Nat. Nanotechnol. **11**, 1071 (2016).

[10] A. B. Taylor and P. Zijlstra, Single-molecule plasmon sensing: Current status and future prospects, ACS Sensors **2**, 1103 (2017).

[11] L. Zhu, A. Fiorino, D. Thompson, R. Mittapally, E. Meyhofer, and P. Reddy, Near-field photonic cooling through control of the chemical potential of photons, Nature (London) **566**, 239 (2019).

[12] R. Gillibert, M. Malerba, D. Spirito, V. Giliberti, L. Li, A. G. Davies, E. H. Linfield, L. Baldassarre, R. Colombelli, and M. Ortolani, Nanospectroscopy of a single patch antenna strongly coupled to a mid-infrared intersubband transition in a quantum well, Appl. Phys. Lett. **117** (2020).

[13] E. Sakat, L. Wojszvzyk, J.-J. Greffet, J.-P. Hugonin, and C. Sauvan, Enhancing light absorption in a nanovolume with a nanoantenna: Theory and figure of merit, ACS Photonics **7**, 1523 (2020).

[14] S. Rajabali, S. Markmann, E. Jöchl, M. Beck, C. A. Lehner, W. Wegscheider, J. Faist, and G. Scalari, An ultrastrongly coupled single terahertz meta-atom, Nat. Commun. **13**, 2528 (2022).

[15] N. Meinzer, W. L. Barnes, and I. R. Hooper, Plasmonic meta-atoms and metasurfaces, Nat. Photonics **8**, 889 (2014).

[16] P. Lalanne and P. Chavel, Metalenses at visible wavelengths: Past, present, perspectives, Laser Photonics Rev. **11**, 1600295 (2017).

[17] C. F. Bohren and D. R. Huffman, *Absorption and Scattering of Light by Small Particles* (John Wiley & Sons, New York, 2008).

[18] I. Staude, A. E. Miroshnichenko, M. Decker, N. T. Fofang, S. Liu, E. Gonzales, J. Dominguez, T. S. Luk, D. N. Neshev, I. Brener *et al.*, Tailoring directional scattering through magnetic and electric resonances in subwavelength silicon nanodisks, ACS Nano **7**, 7824 (2013).

[19] M. Husnik, S. Linden, R. Diehl, J. Niegemann, K. Busch, and M. Wegener, Quantitative experimental determination of scattering and absorption cross section spectra of individual optical metallic nanoantennas, Phys. Rev. Lett. **109**, 233902 (2012).

[20] A. Crut, P. Maioli, N. Del Fatti, and F. Vallée, Optical absorption and scattering spectroscopies of single nano-objects, Chem. Soc. Rev. **43**, 3921 (2014).

[21] G. Baffou, P. Bon, J. Savatier, J. Polleux, M. Zhu, M. Merlin, H. Rigneault, and S. Monneret, Thermal imaging of nanostructures by quantitative optical phase analysis, ACS Nano **6**, 2452 (2012).

[22] J.-J. Greffet, P. Bouchon, G. Brucoli, and F. Marquier, Light emission by nonequilibrium bodies: Local Kirchhoff law, Phys. Rev. X **8**, 021008 (2018).

[23] Y. De Wilde, F. Formanek, R. Carminati, B. Gralak, P.-A. Lemoine, K. Joulain, J.-P. Mulet, Y. Chen, and J.-J. Greffet, Thermal radiation scanning tunnelling microscopy, Nature (London) **444**, 740 (2006).

[24] C. Li, V. Krachmalnicoff, P. Bouchon, J. Jaeck, N. Bardou, R. Haidar, and Y. De Wilde, Near-field and far-field thermal emission of an individual patch nanoantenna, Phys. Rev. Lett. **121**, 243901 (2018).

[25] L. Abou-Hamdan, C. Li, R. Haidar, V. Krachmalnicoff, P. Bouchon, and Y. De Wilde, Hybrid modes in a single thermally excited asymmetric dimer antenna, Opt. Lett. **46**, 981 (2021).

[26] M. Malerba, S. Sotgiu, A. Schirato, L. Baldassarre, R. Gillibert, V. Giliberti, M. Jeannin, J.-M. Manceau, L. Li, A. G. Davies *et al.*, Detection of strong light–matter interaction in a single nanocavity with a thermal transducer, ACS Nano **16**, 20141 (2022).

[27] L. Jauffred, A. Samadi, H. Klingberg, P. M. Bendix, and L. B. Oddershede, Plasmonic heating of nanostructures, Chem. Rev. **119**, 8087 (2019).

[28] J. C. Cuevas and F. J. García-Vidal, Radiative heat transfer, ACS Photonics **5**, 3896 (2018).

[29] W. Li and S. Fan, Nanophotonic control of thermal radiation for energy applications, Opt. Express **26**, 15995 (2018).

[30] M. Makhsiyan, P. Bouchon, J. Jaeck, J.-L. Pelouard, and R. Haïdar, Shaping the spatial and spectral emissivity at the diffraction limit, Appl. Phys. Lett. **107**, 251103 (2015).

[31] D. G. Baranov, Y. Xiao, I. A. Nechepurenko, A. Krasnok, A. Alù, and M. A. Kats, Nanophotonic engineering of far-field thermal emitters, Nat. Mater. **18**, 920 (2019).

[32] L. Wojszvzyk, A. Nguyen, A.-L. Coutrot, C. Zhang, B. Vest, and J.-J. Greffet, An incandescent metasurface for quasimonochromatic polarized mid-wave infrared emission modulated beyond 10 MHz, Nat. Commun. **12**, 1492 (2021).

[33] J. J. García-Esteban, J. Bravo-Abad, and J. C. Cuevas, Tunable thermal emission of subwavelength silica ribbons, ACS Photonics **9**, 3679 (2022).

[34] A. Nguyen, J.-P. Hugonin, E. Garcia-Caurel, A.-L. Coutrot, B. Vest, and J.-J. Greffet, Circularly polarized light emission by incandescent metasurfaces, in *Plasmonics: Design, Materials, Fabrication, Characterization, and Applications XX* (SPIE, Bellingham, 2022), p. PC121970I.

[35] Y. Cui, Y. He, Y. Jin, F. Ding, L. Yang, Y. Ye, S. Zhong, Y. Lin, and S. He, Plasmonic and metamaterial structures as electromagnetic absorbers, Laser Photonics Rev. **8**, 495 (2014).

[36] F. Sterl, E. Herkert, S. Both, T. Weiss, and H. Giessen, Shaping the color and angular appearance of plasmonic metasurfaces with tailored disorder, ACS Nano **15**, 10318 (2021).

[37] S. Ogawa and M. Kimata, Metal-insulator-metal-based plasmonic metamaterial absorbers at visible and infrared wavelengths: A review, Materials **11**, 458 (2018).

[38] M. McCool and E. Fiume, Hierarchical Poisson disk sampling distributions, in *Graphics Interface* (Canadian Information Processing Society, Vancouver, Canada, 1992), Vol. 92, pp. 94–105.

[39] B. Widom, Random sequential addition of hard spheres to a volume, J. Chem. Phys. **44**, 3888 (1966).

[40] S. Torquato and F. H. Stillinger, Local density fluctuations, hyperuniformity, and order metrics, Phys. Rev. E **68**, 041113 (2003).

[41] K. Vynck, R. Pierrat, R. Carminati, L. S. Froufe-Pérez, F. Scheffold, R. Sapienza, S. Vignolini, and J. J. Sáenz, Light in correlated disordered media, Rev. Mod. Phys. **95**, 045003 (2023).

[42] S. Yu, C.-W. Qiu, Y. Chong, S. Torquato, and N. Park, Engineered disorder in photonics, Nat. Rev. Mater. **6**, 226 (2021).

[43] S. Torquato, Hyperuniform states of matter, Phys. Rep. **745**, 1 (2018).

[44] See Supplemental Material at http://link.aps.org/supplemental/10.1103/PhysRevLett.132.043801 for details on fabrication, characterization, electromagnetic modeling, absorption cross section of dipole, and hyperuniformity, which includes Refs. [45–50].

[45] H.-C. Chang and T. Charalampopoulos, Determination of the wavelength dependence of refractive indices of flame soot, Proc. R. Soc. A **430**, 577 (1990).

[46] K. Mizuno, J. Ishii, H. Kishida, Y. Hayamizu, S. Yasuda, D. N. Futaba, M. Yumura, and K. Hata, A black body absorber from vertically aligned single-walled carbon nanotubes, Proc. Natl. Acad. Sci. U.S.A. **106**, 6044 (2009).

[47] R. L. Olmon, B. Slovick, T. W. Johnson, D. Shelton, S.-H. Oh, G. D. Boreman, and M. B. Raschke, Optical dielectric function of gold, Phys. Rev. B **86**, 235147 (2012).

[48] M. Querry, *Optical Constants of Minerals and Other Materials from the Millimeter to the Ultraviolet* (Chemical Research, Development and Engineering Center, U.S. Army Armament, NJ, 1998).

[49] J. P. Hugonin and P. Lalanne, Reticolo software for grating analysis, arXiv:2101.00901.

[50] R. Alaee, M. Albooyeh, and C. Rockstuhl, Theory of metasurface based perfect absorbers, J. Phys. D **50**, 503002 (2017).

[51] M. Striebel, J. Wrachtrup, and I. Gerhardt, Absorption and extinction cross sections and photon streamlines in the optical near-field, Sci. Rep. **7**, 15420 (2017).

[52] E. W. Streed, A. Jechow, B. G. Norton, and D. Kielpinski, Absorption imaging of a single atom, Nat. Commun. **3**, 1 (2012).

[53] S. Tretyakov, Maximizing absorption and scattering by dipole particles, Plasmonics **9**, 935 (2014).

[54] *Introduction to COMSOL Multiphysics*, (COMSOL Multiphysics, Burlington, MA, 1998), accessed February 9, 2018.

[55] E. D. Palik, *Handbook of Optical Constants of Solids* (Academic Press, New York, 1998), Vol. 3.

[56] K. Vynck, R. Pacanowski, A. Agreda, A. Dufay, X. Granier, and P. Lalanne, The visual appearances of disordered optical metasurfaces, Nat. Mater. **21**, 1035 (2022).

Correction: An affiliation indicator was missing from the fourth author's name and has been inserted.